Modeling, Identification and Control, Vol. 45, No. 4, 2024, pp. 115–126, ISSN 1890–1328

Antiswing Control and Trajectory Planning for Offshore Cranes: Design and Experiments

Ronny Landsverk [1] Jing Zhou [1] Daniel Hagen [1]

[1] *Department of Engineering Sciences, University of Agder, 4898 Grimstad, Norway*
E-mails: ronny.landsverk@uia.no@uia.no, jing.zhou@uia.no, daniel.hagen@uia.no

Abstract

In offshore environments, safe management of heavy payloads requires precise crane operations to avoid collisions with obstacles and adjacent equipment. Uncontrolled residual swinging of suspended payloads can quickly evolve into high-risk situations, which, if left unchecked, might lead to significant equipment failures and associated costs. This paper explores a control methodology designed specifically to eliminate payload swing in offshore cranes. We present a trajectory tracking technique explicitly crafted for swing suppression under control, rooted in the principles of the iterative learning algorithm and based on physics. The proposed antiswing control strategy guarantees asymptotic convergence of the payload's swing, angular velocity, and angular acceleration to desired values. The method was tested on a Comau robot mounted on a Stewart platform at the Norwegian Motion Laboratory. Simulation and experimental results comparing payload transfers with and without applying the anti-swing control method validates it's effectiveness.

Keywords: Antiswing control, crane control, modeling, trajectory planning, iterative learning

1 Introduction

Cranes play a pivotal role in the handling and transportation of equipment within offshore industries, such as the drilling, installation, and maintenance of offshore wind farms. Especially in harsh environments, such as the North Sea, ensuring safety is paramount. In extreme situations, a heavy lifting operation can compromise vessel stability, potentially leading to dangerous scenarios and high-cost failures.

Consequently, significant research has been done on the modeling and control of cranes in the past decade. In Fang et al. (2014), a dynamic Lagrangian-based model was introduced for a boom crane mounted on a ship. Subsequent work built on this by emphasizing offshore crane control in Qian and Fang (2016) and Lu et al. (2018). Ellerman et al. (2002) analyzed a moored crane-vessel with suspended load, focusing on non-linear dynamic phenomena influenced by mooring stiffness.

Using Kane's method, Tysse and Egeland (2018) and Cibicik et al. (2019) modeled a fully coupled spatial knuckle-boom crane on a marine craft, employing a minimal set of coordinates and generalized speeds. Here, the partial velocities essential for Kane's equations were defined using screws, facilitating screw transformations for kinetic projection to the inertial frame. Meanwhile, Landsverk et al. (2020) utilized a classical multibody dynamics formulation to derive an exhaustive model of a vessel, crane, and payload, accounting for the full set of Cartesian coordinates, Euler angles for each body, and closed-loop kinetics arising from linear actuators like hydraulic cylinders. For trajectory planning, approaches such as the cycloidal-based motion profiles for manipulators have been proposed for eliminating residual swing of a hanging payload Alici et al. (1999); Gürsel et al. (2000). Effective swing elimination and precision in positioning for

doi:10.4173/mic.2024.4.1

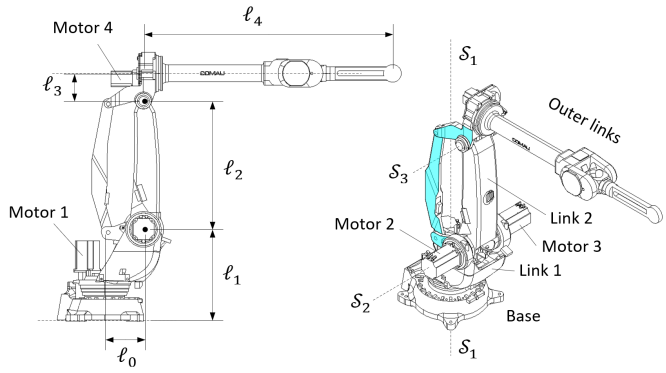

Figure 1: Schematic robot system

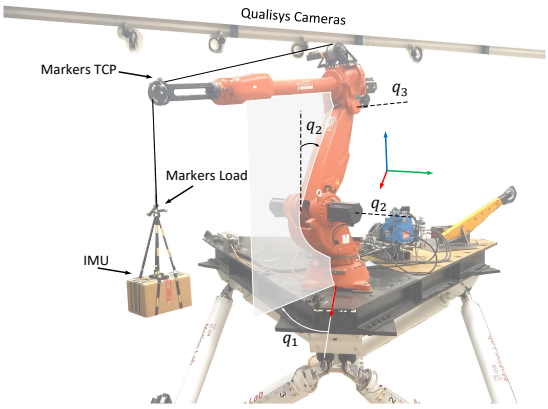

Figure 2: Real Comau Robot

overhead cranes using Lyapunov-based analysis is illustrated in N. Sun and Ma (2012) and Sun and Fang (2014). Furthermore, a blend of input shaping with closed-loop control has been implemented for swing elimination in an offshore boom crane Agostini et al. (2002). Other methods include energy-based nonlinear controls Sun et al. (2018, 2019a); Chen and Sun (2022) and adaptive controls Gao et al. (2019); Sun et al. (2019b); Huang et al. (2022).

In this paper, we implement a trajectory tracking method for suppressing payload swing in open-loop control of offshore cranes. The aim is to swiftly and accurately transport the load to its target location while concurrently minimizing payload swing. Drawing inspiration from an iterative learning algorithm crafted for overhead cranes N. Sun and Ma (2012), our approach utilizes an anti-swing mechanism to shape a smooth reference trajectory. Rapid convergence of the iterative learning makes it suitable for deployment in current offshore crane systems. From an industrial standpoint, this enhances transportation efficiency and bolsters safety in high-risk environments. Notably, our open-loop approach negates the need for sensor feedback from the payload. Through Lyapunov techniques, we demonstrate that the proposed anti-swing control method assures asymptotic convergence of the payload's swing, angular velocity, and angular acceleration. Simulation and experimental outcomes underscore the exceptional performance of this control method. The primary innovation lies in adapting techniques from N. Sun and Ma (2012) for a spatial knuckle boom crane, diverging from the traditional planar overhead crane, as well as expanding it's application from planar to spatial motion.

The paper proceeds as follows: Section II delineates the kinematics of crane systems; Section III introduces the anti-swing control strategy; Section IV appraises the method's efficacy and shares simulation outcomes; Section V shares experimental outcomes and Section VI offers concluding remarks.

2 Modeling of Crane System

In this paper, a closed-chain manipulator of type Comau SmartNJ with an appended winch and wire system is considered. The manipulator will capture the essential dynamics of a typical offshore knuckle-boom crane if two linear actuators are replaced by rotary actuators placed at the joints (see hydraulic cylinders in Landsverk et al. (2020)).

Fig. 1 and Fig. 2 show the considered robot, parameterized by lengths ℓ_i, $i = \{0, 1, 2, 3, 4\}$ and screw axes $\mathcal{S}_j$, $j = \{1, 2, 3\}$. The actuator *Motor 1* is rotating *Link 1* relative to the base about axis $\mathcal{S}_1$ via a gear. The actuator *Motor 3* turns link *Link 2* relative to *Link 1* about axis $\mathcal{S}_2$. For serial kinematic chains the distal links will follow any motion from proximal links, but notice the three links with highlighted faces in the Fig 1. These three links together with *Link 2* forms a parallelogram kinematic mechanism. This closed-chain design increases the stiffness of the robot and leads to a decoupling of kinematics. Also, note that actuator *Motor 2* is rotating the parallel mechanism, whereas the orientation of the outer links stays fixed relative to screw axis $\mathcal{S}_3$. Fig. 3 shows the decoupled behaviour of the outer links when *Motor 2* is actuated while *Motor 3* remains stationary.

To account for the decoupled kinematics, we append a virtual zero-length link that negates the kinematics between *Link 2* and the outer links. Alternatively, we define joint variable $q_3^* = q_3 - q_2$ as a replacement for the joint variable that specifies rotation about axis $\mathcal{S}_3$.

The forward kinematics from the base frame $\{0\}$ to

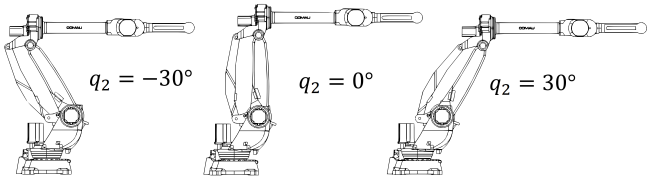

Figure 3: Closed-chain behaviour

the tool frame $\{4\}$ can be written in terms of the screws $\mathcal{S}_i$ and associated joint variables $\mathbf{q}$, as shown in Fig. 1, and Fig. 2 :

$$\mathcal{S}_1 = \begin{bmatrix} \mathbf{w}_1 \\ \mathbf{v}_1 \end{bmatrix}, \mathcal{S}_2 = \begin{bmatrix} \mathbf{w}_2 \\ \mathbf{v}_2 \end{bmatrix}, \mathcal{S}_3 = \begin{bmatrix} \mathbf{w}_3 \\ \mathbf{v}_3 \end{bmatrix}, \mathbf{q} = \begin{bmatrix} q_1 \\ q_2 \\ q_3^* \end{bmatrix}, \quad (1)$$

where $\mathbf{w}_i \in \mathbb{R}^3$ is a unit vector pointing along the screw axis $\mathcal{S}_i \in \mathbb{R}^6$ and $\mathbf{v}_i \in \mathbb{R}^3$ is the negative kinematic moment of the screw axis at an arbitrary point $\mathbf{p}_i \in \mathbb{R}^3$ on the screw axis,

$$\mathbf{v}_i = -\mathbf{w}_i \times \mathbf{p}_i, \qquad i = \{1, 2, 3\}. \quad (2)$$

Then we define the matrix $\mathbf{T} = \mathbf{T}(\mathbf{q}) \in SE(3)$ which acts as the transformation from frame $\{0\}$ to $\{4\}$ in the base frame

$$\mathbf{T}(\mathbf{q}) = \mathbf{exp}(\tilde{\mathcal{S}}_1 q_1)\mathbf{exp}(\tilde{\mathcal{S}}_2 q_2)\mathbf{exp}(\tilde{\mathcal{S}}_3 q_3)\mathbf{T}(\mathbf{0}), \quad (3)$$

where the tilde notation denotes transforming a screw to an element in $se(3)$ - representing the Lie algebra for the special Euclidian group $SE(3)$, and transforms a vector to an element in $so(3)$ - representing the Lie algebra for the special orthogonal group $SO(3)$. Both according to

$$\tilde{\mathcal{S}} = \begin{bmatrix} \tilde{\mathbf{w}} & \mathbf{v} \\ \mathbf{0} & 0 \end{bmatrix} \in se(3), \quad (4)$$

and

$$\tilde{\mathbf{w}} = \begin{bmatrix} 0 & -w_3 & w_2 \\ w_3 & 0 & -w_1 \\ -w_2 & w_1 & 0 \end{bmatrix} \in so(3). \quad (5)$$

The operator **exp** denotes the matrix exponential

$$\mathbf{exp}(\mathbf{A}) = \mathbf{I} + \frac{1}{2!}\mathbf{A}^2 + \cdots + \frac{1}{k!}\mathbf{A}^k + \cdots. \quad (6)$$

Finally, $\mathbf{T}(\mathbf{0})$ denotes the element in $SE(3)$ that describes the pose of frame $\{4\}$ relative to $\{0\}$ when all joint variables are zero. [1]

To implement the antiswing signal, we need to first specify a trajectory for the tool centre point (TCP) of the crane in base frame coordinates, and transform this trajectory from the cartesian tool space to the joint space. Note that the base frame $\{0\}$ is an inertial frame, and the TCP is the origin of frame $\{4\}$. The inverse kinematics can more easily be determined by employing a small trick to account for the offset ℓ_3 between joint 3 and frame $\{4\}$. By defining joint variable $q_3 = q_3^* - \arctan(\ell_3/\ell_4)$ and link length $\ell_5 = \sqrt{\ell_3^2 + \ell_4^2}$ then given any TCP position $\vec{r}_{4/0} = (p_x, p_y, p_z)$, where the notation $\vec{r}_{j/i}$ specifies a geometric vector from frame $\{i\}$ to $\{j\}$, we can write

$$q_1 = \arctan(p_y/p_x). \quad (7)$$

Once we have q_1 we can rotate the TCP vector $\vec{r}_{4/0}$ by angle $(-q_1)$ about $\vec{k}$ such that the robot aligns with the base x axis. This effectively will turn the vector $\vec{r}_{4/0}$ into a planar vector in the (x, z)-plane, and using Fig. 4 we write

$$\vec{r}_{4/2} = \vec{r}_{4/0} - \vec{r}_{2/0} = (r_x, r_z). \quad (8)$$

Then we can use the law of cosines to find the angle q_2. Finally, using the rightmost picture of Fig. 4, we get the relations

$$\frac{\pi}{2} + q_2 = \theta + \phi, \qquad \frac{\pi}{2} + q_3 = \psi, \quad (9)$$

where

$$\phi = \arccos\left(\frac{\ell_2^2 + \ell_6^2 - \ell_5^2}{2\ell_2\ell_6}\right), \quad (10)$$

and

$$\psi = \arccos\left(\frac{\ell_2^2 + \ell_5^2 - \ell_6^2}{2\ell_2\ell_5}\right), \quad (11)$$

where $\ell_6 = \sqrt{r_x^2 + r_z^2}$ and $\theta = \arctan(r_z/r_x)$. Note that we also need to account for poses that have two equally valid solutions in joint space, i.e. elbow up.

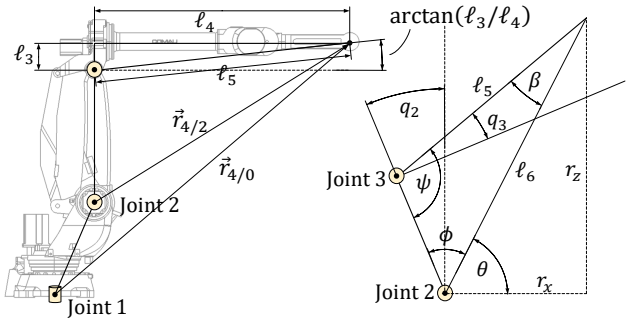

Figure 4: Inverse kinematics

For the relation between TCP velocity $\mathbf{v} = \dot{\mathbf{r}}$ and joint velocities $\dot{\mathbf{q}}$, where $\dot{\mathbf{r}}$ is the time derivative of the

[1] The zero-pose for the physical Comau robot has link 3 pointing vertically upwards

algebraic form of the vector $\vec{r}_{4/0}$, we need to derive the Jacobian matrix $\mathbf{J} = \mathbf{J}(\mathbf{q})$

$$\mathbf{v} = \mathbf{J}(\mathbf{q})\dot{\mathbf{q}}. \tag{12}$$

The overall Jacobian can be interpreted as a collection of matrices that describe kinematic contributions from each joint

$$\mathbf{J} = \begin{bmatrix}\mathbf{J}_1 & \mathbf{J}_2 & \mathbf{J}_3\end{bmatrix} \in \mathbb{R}^{3\times 3}, \tag{13}$$

where each unit describes a cross product

$$\mathbf{J}_i = \mathbf{w}_i \times (\mathbf{r} - \mathbf{r}_{i/0}), \qquad i = \{1, 2, 3\}, \tag{14}$$

where $\mathbf{r}_{i/0}$ denotes the vector from frame $\{0\}$ to $\{i\}$, expressed in frame $\{0\}$ coordinates. Furthermore $\mathbf{r} = \mathbf{r}_{4/0}$, and $\mathbf{w}_i$ is a unit vector in the positive direction along the axis of joint i, also in frame $\{0\}$ coordinates. Differentiating Eq. (12) with respect to time yields

$$\dot{\mathbf{v}} = \frac{\partial \mathbf{J}}{\partial \mathbf{q}}\dot{\mathbf{q}}^2 + \mathbf{J}(\mathbf{q})\ddot{\mathbf{q}} = \mathbf{C}(\mathbf{q}, \dot{\mathbf{q}})\dot{\mathbf{q}} + \mathbf{J}(\mathbf{q})\ddot{\mathbf{q}}. \tag{15}$$

As kinematics is linear in velocity and acceleration, and since the Jacobian is square in our interval of interest, it follows that inverse kinematics for velocities and accelerations may follow directly from equations (12) and (15) while keeping the workspace within this interval.

3 Antiswing Control

The control objective is to accurately position the TCP from a point A to a point B in a specified time T_f - starting and ending the trajectory with zero velocity and acceleration - while simultaneously suppressing the residual swing from the hanging load.

3.1 Trajectory Planning

Fig. 5 depicts a situation where a hanging load is moved from point A to point B along a horizontal straight line.

The plane in the figure highlights that the pendulum dynamics is essentially planar and assuming no friction, the governing equation for the payload can be written

$$m\ell\ddot{s}\cos(\theta) + m\ell^2\ddot{\theta} = -mg\ell\sin(\theta), \tag{16}$$

where m is the payload mass, ℓ is the pendulum length, g is the gravitational constant, and θ and s are state variables. Note that s is the distance along the line $s_B - s_A = \|\mathbf{r}_B - \mathbf{r}_A\|$ where $\mathbf{r}_A$ is the component vector for $\vec{r}_{4/0}$ when the TCP is located at point A and similarly for $\mathbf{r}_B$. Dividing Eq. (16) by $m\ell$ yields the equation

$$\ell\ddot{\theta} + \ddot{s}\cos(\theta) + g\sin(\theta) = 0. \tag{17}$$

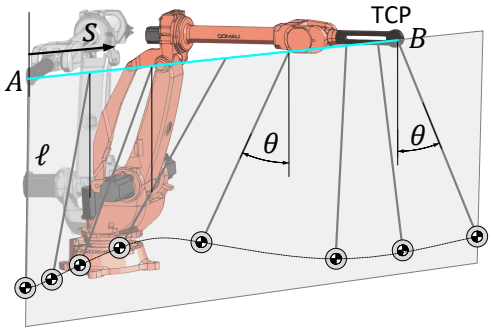

Figure 5: Crane and payload

Eq. (17) forms the basis for designing a swing elimination signal - hereby denoted as the antiswing signal. The primary control goal is for the TCP position s to reach a specified position p without overshoot in time T_f. The state s and it's derivatives up to third order must be uniformly bounded with $\dot{s} \geq 0$, $|\ddot{s}| < g$ and $\dot{s}(T_f) = \ddot{s}(T_f) = 0$.

3.2 Antiswing Signal

First, we specify a linear filter

$$\sigma = \dot{\theta} + \alpha\theta, \tag{18}$$

where $\alpha \in \mathbb{R}$, and define the antiswing signal as

$$\ddot{s}_a = \frac{-g\sin(\theta) + \alpha\ell\dot{\theta} + \beta\sigma}{\cos(\theta)}, \tag{19}$$

where $\beta \in \mathbb{R}$. The TCP reference trajectory is combined with the anti-swing signal as

$$\ddot{s} = \ddot{s}_{\text{ref}} + \gamma\ddot{s}_a, \tag{20}$$

where $\gamma \in \mathbb{R}$ is a gain factor and $\ddot{s}_{\text{ref}}$ is a smooth trajectory acceleration reference. By taking the derivative of the filter (Eq. 18) and using the dynamics in Eqs. (17), (19), the filter can be written as $\sigma = C \cdot e^{-\beta t/\ell}$, which shows that $\theta, \dot{\theta}$ decays exponentially fast. Based on the analysis N. Sun and Ma (2012), using Lyapunov function

$$V(t) = \frac{1}{2}\ell\dot{\theta}^2 - g\left[(\right]1 - \cos(\theta)\right], \tag{21}$$

and Barbalat's lemma, the antiswing signal (19) and the reference trajectory (20) can be shown to suppress the payload swing successfully and efficiently. The results are shown in the following theorem.

Theorem 1 *The combined anti-swing mechanism (19) and the reference trajectory (20) guarantee asymptotic convergence of the swing, the angular velocity, and the angular acceleration of the payload, such that*

$$\lim_{t\to\infty}\left(\theta(t), \dot{\theta}(t), \ddot{\theta}(t)\right) = (0, 0, 0). \tag{22}$$

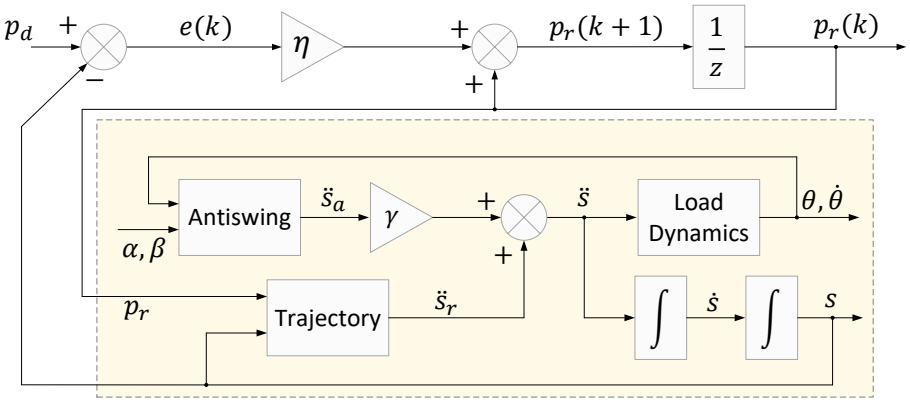

Figure 6: Iterative learning

Proof: The results are obtained using Lyapunov techniques, Barbalat's lemma and extended Barbalat's lemma. More detailed analysis is given in N. Sun and Ma (2012).

The system shown in Fig. 6 shows the iterative learning algorithm, where the highlighed subsystem makes up a single iteration of the iterative learning procedure.

3.3 Iterative Learning

The block *Antiswing* consists of the antiswing signal, dependent on parameters α, β and state variables θ and $\dot{\theta}$. The block *Trajectory* is responsible for generating a smooth trajectory for the TCP, e.g. a quintic polynomial in s_r with boundary conditions $\dot{s}_r(0) = \ddot{s}_r(0) = \dot{s}_r(T_f) = \ddot{s}_r(T_f) = 0$. The block is dependent on the parameters p_r, T_f, and state variable s. Note that T_f is a constant, and p_r is an optimization variable for the algorithm. The block *Load Dynamics* consists of the pendulum dynamics (17), and is straightforward. The algorithm is utilizing the sub-system shown in Fig. 6 for each iteration k. The error $e(k)$ is the difference between the desired final position $s(T_f) \approx p_d$ and the final position of the previous step, denoted by $s(k, T_f)$,

$$e(k) = p_d - s(k, T_f). \tag{23}$$

The variable $p_r(k)$ is used as a total displacement-input for the trajectory generator during iteration k, and gets updated for the next iteration by

$$p_r(k+1) = \eta e(k) + p_r(k), \tag{24}$$

where η governs the rate of convergence. It's easy to see that as $e(k) \to 0$, the iterative algorithm stabilizes for a suitable $p_r(k+1) \approx p_r(k)$.

3.4 Antiswing for a Spherical Pendulum

For payload transfers where obstacles prevent linear point-to-point motion (see Fig. 7), the hanging payload acts as a spherical pendulum with a moving attachment point. Using Fig. 8, we write the position vector of the

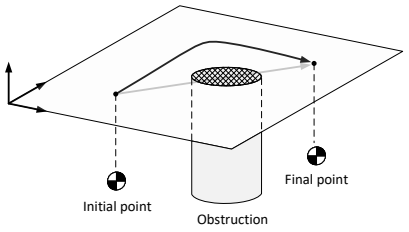

Figure 7: Path inducing coordinate coupling

payload as

$$\mathbf{p} = \mathbf{r}_4 + \mathbf{R} \begin{bmatrix} 0 \\ 0 \\ -\ell \end{bmatrix}, \tag{25}$$

where $\mathbf{r}_4$ is the position vector of the attachment point in the base frame and $\mathbf{R}$ is the rotation matrix $\mathbf{R} = \mathbf{R}_z(\varphi_2)\mathbf{R}_y(-\varphi_1)$. Note that we assume that frame $\{4\}$ is initially coincident with a global inertial coordinate system, and the order of the matrix multiplication indicates that the state variables φ_1, φ_2 are relative to that global frame.

The equations of motion for the system can be derived based on the system energy

$$E_k = \frac{m}{2}\mathbf{v}^T\mathbf{v}, \qquad E_p = mg\ell(1 - \cos(\varphi_1)), \tag{26}$$

where m, g, ℓ are mass, gravity and length, and where $\mathbf{v} = d\mathbf{p}/dt$ is the pendulum velocity. The equations of

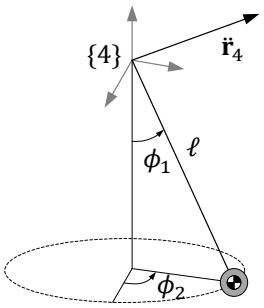

Figure 8: A spherical pendulum

motion may be found by the Euler-Lagrange equation

$$\frac{d}{dt}\frac{\partial \mathcal{L}}{\partial \dot{\varphi}_i} - \frac{\partial \mathcal{L}}{\partial \varphi_i} = \tau_i, \qquad i = \{1, 2\} \tag{27}$$

where $\mathcal{L} = E_k - E_p$. The right-hand side τ_i is zero in both cases here. The final equations of motion - where we denote $\sin(\varphi_i)$ and $\cos(\varphi_i)$ by s_i and c_i, respectively, can be written

$$m\ell f_1(\varphi_1, \varphi_2, \dot{\varphi}_1, \dot{\varphi}_2, \ddot{\varphi}_1, \ddot{\varphi}_2, \ddot{x}, \ddot{y}) = 0 \tag{28}$$
$$m\ell f_2(\varphi_1, \varphi_2, \dot{\varphi}_1, \dot{\varphi}_2, \ddot{\varphi}_1, \ddot{\varphi}_2, \ddot{x}, \ddot{y}) = 0 \tag{29}$$

where

$$f_1 = \ell\ddot{\varphi}_1 + gs_1 - \ell c_1 s_1 \dot{\varphi}_2 + c_1 c_2 \ddot{x} + c_1 s_2 \ddot{y}$$

and

$$f_2 = \ell s_1^2 \ddot{\varphi}_2 + 2\ell c_1 s_1 \dot{\varphi}_1 \dot{\varphi}_2 + s_1 c_2 \ddot{y} - s_1 s_2 \ddot{x}$$

and where $\ddot{x}$ and $\ddot{y}$ are components of $\ddot{\mathbf{r}}_4$, i.e. accelerations of the attachment point and where we assume that $\ddot{z} = 0$. Solving for $\ddot{x}$ and $\ddot{y}$ yields

$$\ddot{x} = \frac{\ell s_1 c_1 c_2 \dot{\varphi}_2^2 + 2\ell c_1^2 s_2 \dot{\varphi}_1 \dot{\varphi}_2 - \ell c_2 \ddot{\varphi}_1}{c_1} + \frac{\ell s_1 c_1 s_2 \ddot{\varphi}_2 - g s_1 c_2}{c_1}, \tag{30}$$

$$\ddot{y} = \frac{\ell s_1 c_1 s_2 \dot{\varphi}_2^2 - 2\ell c_1^2 c_2 \dot{\varphi}_1 \dot{\varphi}_2 - \ell s_2 \ddot{\varphi}_1}{c_1} - \frac{\ell s_1 c_1 c_2 \ddot{\varphi}_2 + g s_1 s_2}{c_1}. \tag{31}$$

As for the one-dimensional pendulum, we define linear filters for x and y in terms of the swing angle φ_1

$$\sigma_x = \dot{\varphi}_1 + \alpha_x \varphi_1, \tag{32}$$

$$\sigma_y = \dot{\varphi}_1 + \alpha_y \varphi_1, \tag{33}$$

and specify antiswing signals

$$\ddot{x}_a = \frac{-g\sin(\varphi_1) - \alpha_x \ell \dot{\varphi}_1 + \beta_x \sigma_x}{\cos(\varphi_1)}, \tag{34}$$

$$\ddot{y}_a = \frac{-g\sin(\varphi_1) - \alpha_y \ell \dot{\varphi}_1 + \beta_y \sigma_y}{\cos(\varphi_1)}. \tag{35}$$

Taking the time derivative of the filters and applying the antiswing signals yields

$$\frac{d\sigma_x}{dt} = -\frac{\beta_x \sigma_x}{\ell} - \frac{\ddot{y}\cos(\varphi_1)\sin(\varphi_2)}{\ell}, \tag{36}$$

and

$$\frac{d\sigma_y}{dt} = -\frac{\beta_y \sigma_y}{\ell} - \frac{\ddot{x}\cos(\varphi_1)\sin(\varphi_2)}{\ell}. \tag{37}$$

The kinematic coupling introduced by the additional terms involves $\ddot{y}$ for σ_x and $\ddot{x}$ for σ_y. These become immaterial as they are both zero at the final point, i.e. when $\mathbf{r}_4(t) = \mathbf{r}_4(T)$. Since the mathematical model is frictionless, any residual swing would persist indefinitely. However, the duration T, during which the coupling terms are nonzero, is negligable compared to the timescale of asymptotic convergence described in Theorem 1. Consequently, the temporary presence of these terms does not impact the results from the theorem.

4 Simulation Results

4.1 Implementing Anti-swing in Cartesian 3-Space

As a specific case for our model, we choose an initial pose of $q_1 = 40°$, $q_2 = -30°$ and $q_3 = -90°$. Suppose we want to move the TCP by a distance of $(s_B - s_A) = \delta s = \sqrt{\delta x^2 + \delta y^2 + \delta z^2}$ along the $y = x$ direction while keeping the z-component constant. Then $\delta s = \sqrt{\delta x^2 + \delta x^2}$. Choosing $\delta s = 2$ m we get $\delta x = \delta y = \sqrt{2}$ m and $\delta z = 0$. For lengths $\ell_0 = 0.35$ m, $\ell_1 = 0.83$ m, $\ell_2 = 1.16$ m, $\ell_3 = 0.25$ m, and $\ell_4 = 2.27$ m, we get the following endpoints $\mathbf{r}_A$ and $\mathbf{r}_B$:

$$\mathbf{r}_A = \begin{bmatrix} 1.56 \\ -1.31 \\ 2.08 \end{bmatrix}, \qquad \mathbf{r}_B = \mathbf{r}_A + \begin{bmatrix} \delta x \\ \delta y \\ 0 \end{bmatrix}.$$

The joint position values that correspond to the pose at $\mathbf{r}_B$ are $q_1 = -2.0°$, $q_2 = 17.6°$, and $q_3 = -92.6°$.

4.2 Simulation results

To test the effectiveness of the anti-swing control, we compare the swing attenuation for a fifth-order poly-

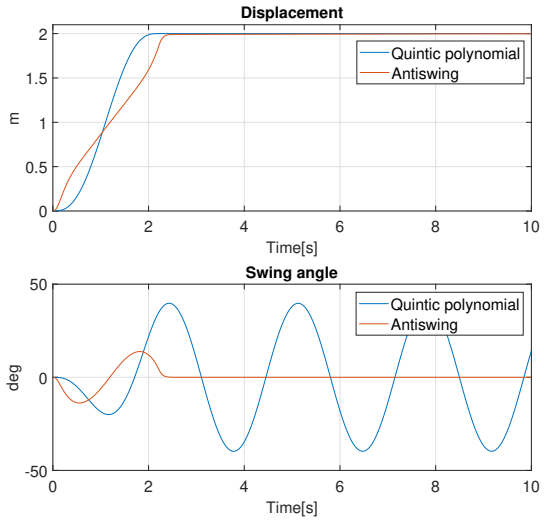

Figure 9: TCP displacement and payload swing angle

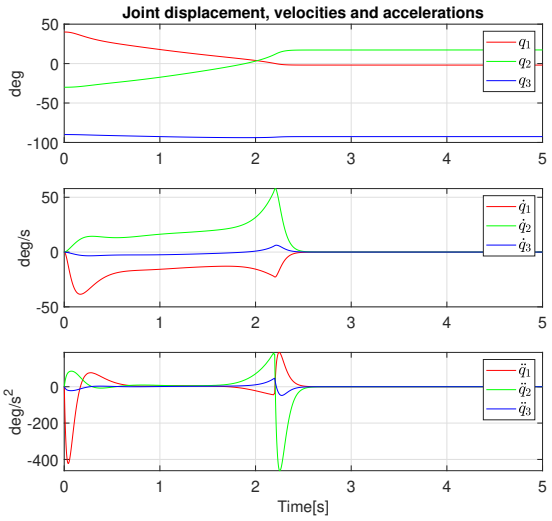

Figure 10: Joint positions, velocities and accelerations

nomial trajectory

$$\begin{aligned} s(t) &= a_0 + a_1 t + a_2 t^2 + a_3 t^3 + a_4 t^4 + a_5 t^5 \\ \dot{s}(t) &= a_1 + 2a_2 t + 3a_3 t^2 + 4a_4 t^3 + 5a_5 t^4 \\ \ddot{s}(t) &= 2a_2 + 6a_3 t + 12a_4 t^2 + 20a_5 t^3 \end{aligned} \tag{38}$$

with $s(0) = \dot{s}(0) = \dot{s}(2.3) = \ddot{s}(0) = \ddot{s}(2.3) = 0$ and $s(2.3) = p_d = 2$, against a trajectory where the antiswing signal is included.

The TCP displacement along s is shown in the upper plot and the payload swing angle is shown in the lower plot of Fig. 9. The red and blue lines are simulation results with and without the antiswing signal. We see that the residual swing is effectively eliminated during the positioning of the payload, which is at a final position at time $t \approx 2.3$ sec. Note that the so-called *smooth* polynomial trajectory will yield a $\pm 45°$ swinging motion lasting forever in a friction-less environment. Fig. 13 shows the error $e(k) = p_d(k) - s(k, T_f)$ for iterations $k = 1, 2, ..., 20$ with a learning rate $\eta = 3.5$. Furthermore, the parameters α, β and γ in equations (18), (19) and (20) are chosen rather randomly as $\alpha = \beta = 20$ and $\gamma = 0.3$. Further recommendations for choosing suitable numbers can be found in N. Sun and Ma (2012).

The effectiveness and validity of the implementation of the antiswing signal to the crane system, and the system modeling shown in this paper, are verified by feeding trajectory references derived from the modeling as joint references for a physical Comau robot. Based on the cartesian trajectory that realizes the aforementioned TCP displacement in Fig. 9, we find trajectories in the joint space as shown in Fig. 10. The joint positions $\mathbf{q}(t) \in \mathbb{R}^3$ are readily found using the inverse kinematics from Eqs. (7), (9), (10) and (11), based on the desired starting TCP position $\mathbf{r}(0) = \mathbf{r}_A$ and the chosen direction of path variable s. The joint velocities and accelerations are calculated using

$$\dot{\mathbf{q}}(t) = \mathbf{J}^{-1}(\mathbf{q}(t))\mathbf{v}(t), \tag{39}$$

for velocity and

$$\ddot{\mathbf{q}}(t) = \mathbf{J}^{-1}(\mathbf{q}(t)) \left[\dot{\mathbf{v}}(t) - \mathbf{C}\left(\mathbf{q}(t), \dot{\mathbf{q}}(t)\right) \dot{\mathbf{q}}(t)\right], \tag{40}$$

for acceleration, where $\mathbf{J} \in \mathbb{R}^{3\times3}$ and $\mathbf{C} \in \mathbb{R}^{3\times3}$ are the geometric Jacobian and it's partial derivative, and $\mathbf{v} \in \mathbb{R}^3$, $\dot{\mathbf{v}} \in \mathbb{R}^3$ are the velocity and acceleration of the TCP in cartesian 3-space. The joint references for position, velocity and acceleration are tested for validity by applying them to the physical robot.

4.3 Antiswing for a Spherical Pendulum

For the case where a straight line path is obstructed, we carry out the iterative learning process in both the x and the y dimensions. Hence, we get a trajectory s_x and s_y, completely analogous to the single dimensional case, but where the trajectories are displaced relative to one another in time. Fig. 11 shows the 3D trajectory of the TCP and the corresponding trajectory of the payload when no antiswing signal is applied. The trajectory starts from the origin $(0, 0, 0)$ and ends at the point $(2, 2, 0)$ in three seconds following a quintic polynomial trajectory in x and y directions. Fig. 12 shows the same trajectories when the antiswing signals are applied.

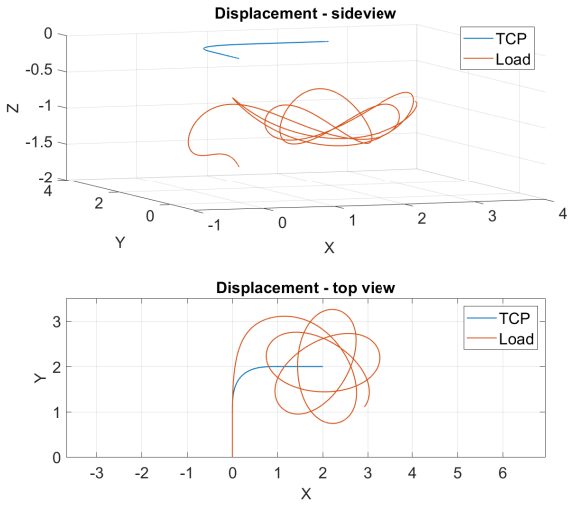

Figure 11: Simulation results: no antiswing

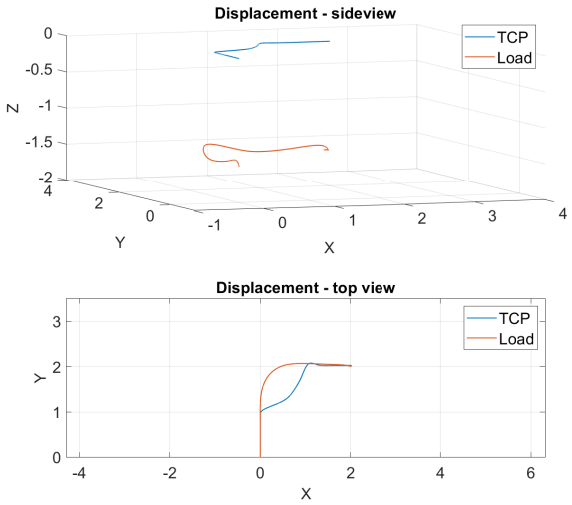

Figure 12: Simulation results: antiswing enabled

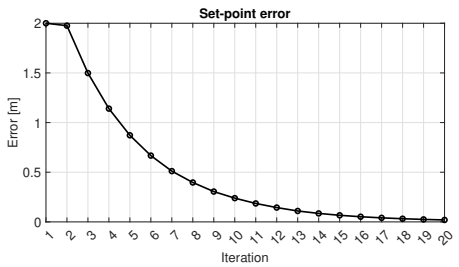

Figure 13: Setpoint error vs iterations

5 Experimental Results

The experimental setup features a Comau robot model Smart-5 NJ-110, mounted on a frame and secured to a Stewart platform in the Norwegian Motion Labotory at the University of Agder (UiA Motion Lab), Grimstad, Norway Tørdal et al. (2018). The robot is equipped with a winch system, introducing dynamic uncertainties related to wire-sheave friction, wire flexibility, and air resistance on the load. Fig. 1 shows the relevant dimensions used when modeling the system. The physical lengths are $\{0.35, 0.83, 1.16, 0.25, 2.27\}$ in meters for $\{\ell_0, ..., \ell_4\}$. An actual photograph of the robot is shown in Fig. 2. A load is suspended from the winch, with its orientation monitored using an Adafruit IMU featuring the Bosch BNO055 sensor. Data is collected via a Raspberry Pi powered by a power bank placed on top of the payload. The IMU communicates over I2C with the Raspberry Pi, which is wirelessly connected to the host PC through SSH. Additionally, UiA Motion Lab is equipped with a Qualisys motion capture system comprising seventeen infrared cameras. Reflective markers are placed at points of interest. The Qualisys Track Manager (QTM) software calculates the spatial positions of these markers relative to a predefined coordinate system. In this experiment, four markers were placed near the robot's tool center point, while another four were attached to the load.

The motion of the Comau robot is controlled by sending joint velocity references through a UDP real-time interface. A Speedgoat real-time target is connected to a UDP server on the Comau computer, allowing control from a Windows host PC via the Speedgoat. Kinematics and antiswing reference velocities are calculated on the Windows host and applied to the Comau robot in an open-loop configuration. Each motor of the Comau robot is managed by an internal speed controller, utilizing field-oriented control with encoder feedback to maintain precise velocity control.

5.1 Antiswing Experimental results

For the first test, we move the payload from an initial point $\mathbf{q} = (0, -40, -85)$ degrees to a final point $\mathbf{q} = (-36.6, 27.6, -88.5)$ degrees, corresponding to a displacement by $\delta\mathbf{r} = (0.684, 1.879, 0)$ meters which displaces the TCP by a distance of 2.0 meters along $\theta = 70°$ relative to x-axis of the robot. The resulting swing angle is measured using the IMU. The results are shown in Fig. 14 where the horizontal axis represents time in seconds, while the vertical axis denotes the swing angle of the load in degrees. The upper plot illustrates the swing angle with and without the antiswing algorithm in simulation, and the lower plot displays corresponding experimental data, measured using the BNO055 IMU sensor. The peak residual swing

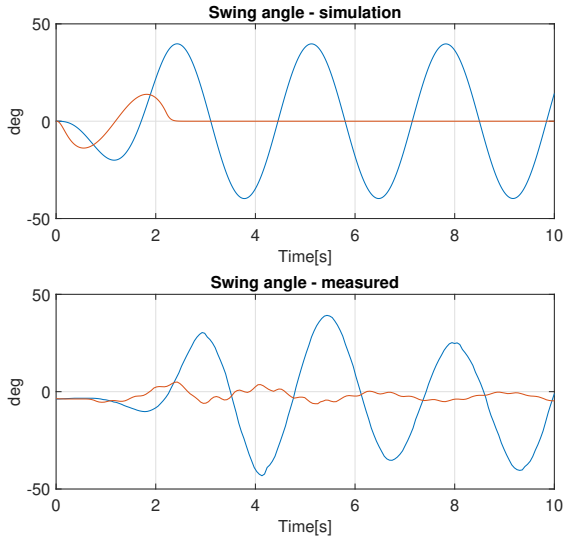

Figure 14: BNO055 IMU Data: Simulation vs experiment

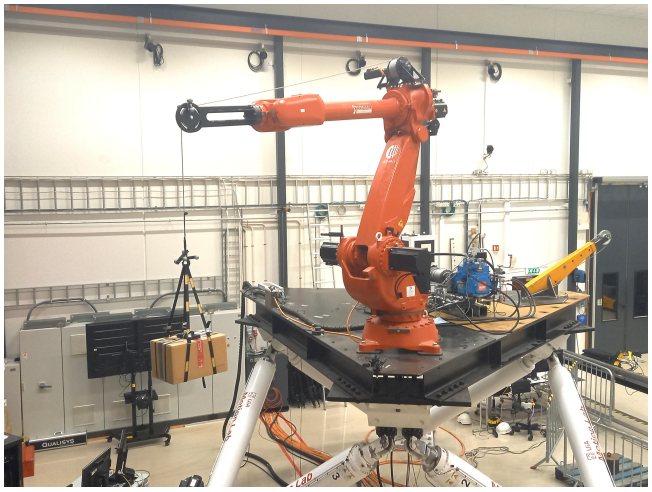

Figure 15: Real Comau robot in UiA Motion Lab

angle measured with the IMU is 42.3 degrees and 2.9 degrees with and without the antiswing, respectively.

Recall that the simulated data is from a frictionless environment whereas the experimental data is not. Therefore we expect similar payload swing behaviour only for a brief time period as shown in the figure.

Data captured with the Qualisys motion capture system during the same experiment are shown in figures 16 and 17. Fig. 16 shows the measured TCP and payload displacements and the applied joint velocities used to realize the motion without the antiswing algorithm. The corresponding data for the same experiment with the antiswing algorithm engaged is shown in Fig. 17. The plots illustrate the differences in motion between the two scenarios, highlighting the effectiveness of the antiswing algorithm in reducing swing and improving positional stability during the displacement. The same positional data for test 1 measured by Qualisys is also presented in Fig. 18, for which antiswing is disabled, and in Fig. 19, where the antiswing algorithm is enabled. The figure illustrates the trajectories of both the TCP and the suspended payload, comparing the motion with and without the application of the antiswing algorithm. This comparison highlights the effectiveness of the antiswing algorithm in minimizing oscillations and achieving smoother motion during the displacement. With the antiswing algorithm engaged, the trajectory of the payload follows the TCP more closely, demonstrating reduced swing and improved positional stability relative to the uncontrolled case.

5.2 Spherical Pendulum

For experiments where straight line payload motion is obstructed, Fig. 20 and Fig. 21 illustrate the experimental data for the spherical antiswing control. In this test the tool center point (TCP) is displaced from the initial position at $(0, 0, 0)$ to the target position at $(1, 1, 0)$ over a duration of three seconds. These figures display the spatial displacement of the TCP and the resulting motion of the payload, clearly demonstrating the significant reduction in payload swing. The corresponding residual swing angles are $\varphi_1 \approx 18°$ for data in Fig. 20 and $\varphi_1 \approx 3°$ for data in Fig. 21. These results support our conclusions in previous sections, specifically that Theorem 1 holds for the coupled dynamics introduced when handling spherical pendulum and confirms the algorithms effectiveness in reducing residual swing even in cases where perfect linear motion is unattainable.

6 Conclusion

In this paper, a control methodology is developed to eliminate payload swing in offshore cranes using iterative learning algorithm. This paper presents the adaptation and experimental implementation of the developed iterative control algorithm developed for offshore cranes. It extends existing antiswing control methods to accommodate spherical pendulums, demonstrating effective reduction of residual swinging motion in both simulations and physical experiments. Simulation results show perfect antiswing with zero residual

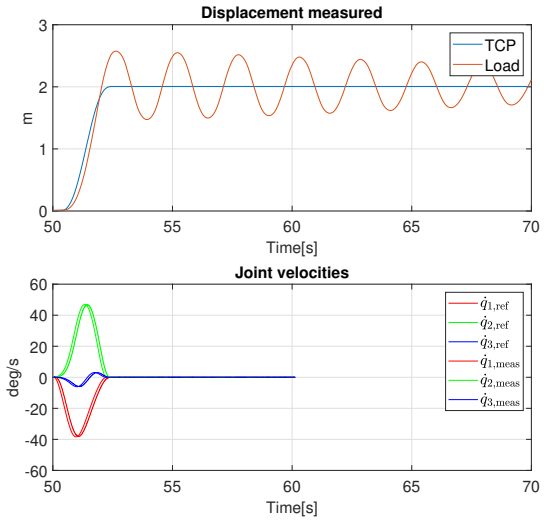

Figure 16: Experimental results: no antiswing

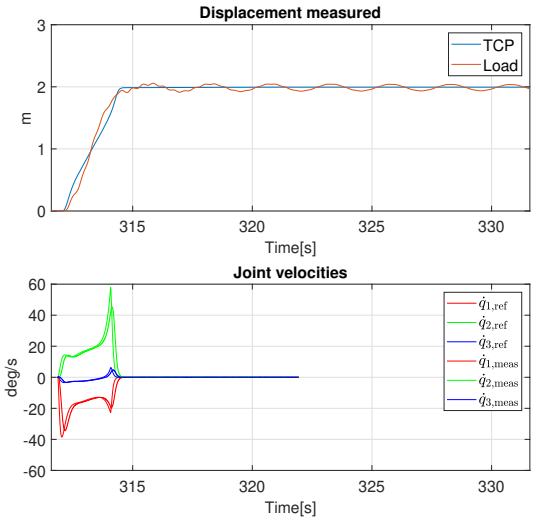

Figure 17: Experimental results: with antiswing

swing. Although unmodeled dynamics often introduce discrepancies, in this case, adding a spherical joint between the TCP and the wire is expected to achieve near-ideal antiswing performance for physical payloads as well.

Future work will extend the developed algorithm to enable realistic antiswing compensation for an offshore vessel-mounted crane, compensating for disturbances from wave motion. Experimental results confirm that the payload wire experiences twisting due to the robot's rotation along the trajectory, an inherent effect that should be addressed in future refinements of the control approach.

Acknowledgments

The work was partially supported from the Research Council of Norway, under SFI Offshore Mechatronics (Grant number 237896) and DEEPCOBOT project (Grant number 306640).

References

Agostini, M., Parker, G., Groom, K., Schaub, H., and Robinett, R. Command Shaping and Closed-Loop Control Interactions for a Ship Crane. *Proceedings of the 2002 American Control Conf.*, 2002. 5:2298–2304. doi:10.1109/ACC.2002.1023983.

Alici, G., Kapucu, S., and Bayseç, S. Swing-free transportation of suspended objects with robot manipulators. *Robotica*, 1999. 17(5):513–521. doi:10.1017/S0263574799001666.

Chen, H. and Sun, N. An Output Feedback Approach for Regulation of 5-DOF Offshore Cranes with Ship Yaw and Roll Perturbations. *IEEE Transactions on Industrial Electronics*, 2022. 69(2):1705–1716. doi:10.1109/TIE.2021.3055159.

Cibicik, A., Tysse, G., and Egeland, O. Determination of Reaction Forces of a Deck Crane in Wave Motion Using Screw Theory. *Journal of Offshore Mechanics and Arctic Engineering*, 2019. 141:1–12. doi:10.1115/1.4043701.

Ellerman, K., Kreuzer, E., and Markiewitcz, M. Nonlinear Dynamics of Floating Cranes. *Nonlinear Dynamics*, 2002. 27:377–387. doi:10.1023/A:1014256405213.

Fang, Y., Wang, P., Sun, N., and Zhang, Y. Dynamic Analysis and Nonlinear Control of an Offshore Boom Crane. *IEEE Transactions on Industrial Electronics*, 2014. pages 414–426. doi:10.1109/TIE.2013.2251731.

Gao, J., Wang, L., Gao, R., and Huang, J. Adaptive control of uncertain underactuated cranes with a non-recursive control scheme. *Journal of the Franklin Institute*, 2019. 356(18):11305–11317. doi:10.1016/j.jfranklin.2019.08.009.

Gürsel, A., Kapucu, S., and Bayseç, S. On preshaped reference inputs to reduce swing of suspended objects transported with robot manipulators. *Mechatronics*, 2000. 10(6):609–626. doi:10.1016/S0957-4158(99)00092-6.

Huang, J., Wang, W., and Zhou, J. Adaptive Control Design for Underactuated Cranes With Guar-

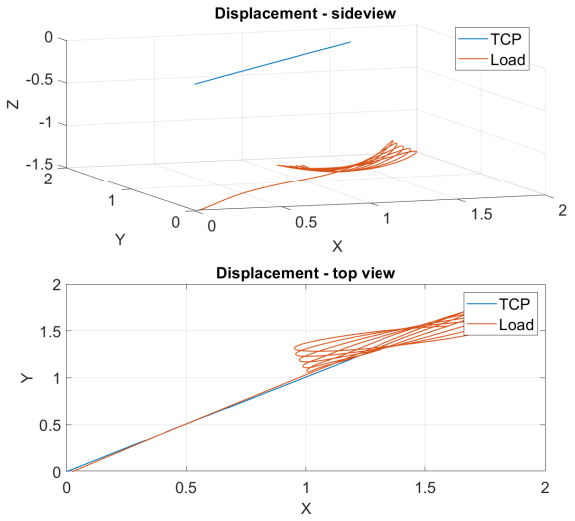

Figure 18: Qualisys data - test 1: no antiswing

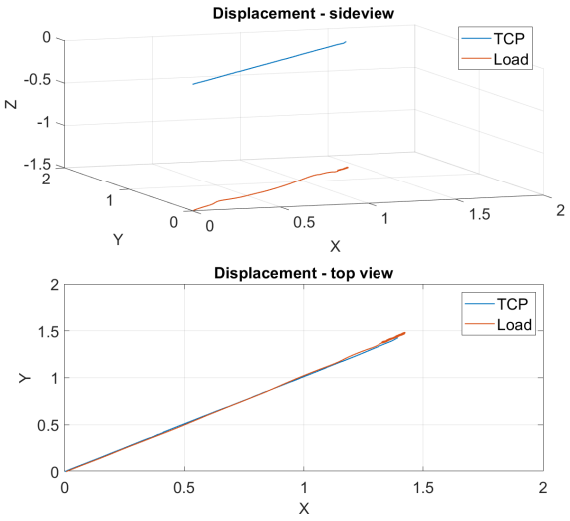

Figure 19: Qualisys data - test 1: with antiswing

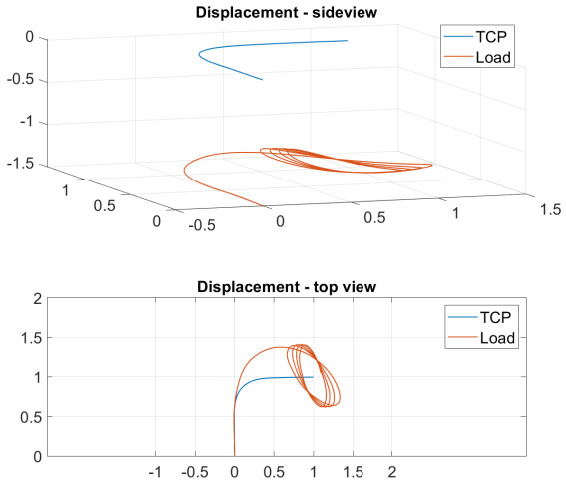

Figure 20: Qualisys data - test 2: no antiswing

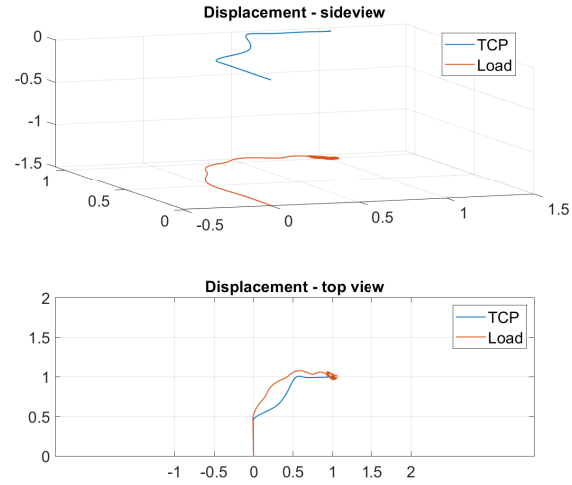

Figure 21: Qualisys data - test 2: with antiswing

anteed Transient Performance: Theoretical Design and Experimental Verification. *IEEE Transactions on Industrial Electronics*, 2022. 69(3):2822–2832. doi:10.1109/TIE.2021.3065835.

Landsverk, R., Zhou, J., Hovland, G., and Zhang, H. Modeling of Offshore Crane and Marine Craft in Wave Motion. *15th IEEE Conference on Industrial Electronics and Applications (ICIEA)*, 2020. pages 1463–1470. doi:10.1109/ICIEA48937.2020.9248110.

Lu, B., Fang, Y., Sun, N., and Wang, X. Antiswing Control of Offshore Boom Cranes with Ship Roll Distrurbances. *IEEE Transactions on Control Systems Technology*, 2018. pages 740–747. doi:10.1109/TCST.2017.2679060.

N. Sun, Y. Z., Y. Fang and Ma, B. A Novel Kinematic Coupling-Based Trajectory Planning Method for Overhead Cranes. *IEEE Transactions on Mechatronics*, 2012. doi:10.1109/TMECH.2010.2103085.

Qian, Y. and Fang, Y. Dynamic Analysis of an Offshore Ship-mounted Crane Subject to Sea Wave Disturbances. *IEEE World Congress on Intelligent Control and Automation*, 2016. pages 1251–1256. doi:10.1109/WCICA.2016.7578629.

Sun, N. and Fang, Y. An efficient online trajectory

generating method for underactuated crane systems. *Int. J. Robust Nonlinear Control*, 2014. 24:1653–1663. doi:10.1002/rnc.2953.

Sun, N., Wu, Y., Fang, Y., and Chen, H. Nonlinear Antiswing Control for Crane Systems with Double-Pendulum Swing Effects and Uncertain Parameters: Design and Experiments. *IEEE Transactions on Automation Science and Engineering*, 2018. 15(3):1413–1412. doi:10.1109/TASE.2017.2723539.

Sun, N., Wu, Y., and Xiao, L. Nonlinear Stable Transportation Control for Double-Pendulum Shipboard Cranes with Ship-Motion-Induced Disturbances. *IEEE Transactions on Industrial Electronics*, 2019a. 66(12):9467–9479. doi:10.1109/TIE.2019.2893855.

Sun, N., Yang, T., Chen, H., Fang, Y., and Qian, Y. Adaptive anti-awing and positioning control for 4-dof rotary cranes subject to uncertain/unknown parameters with hardware experiments. *IEEE Transactions on Systems, Man, and Cybernetics: Systems*, 2019b. 49:1309–1321. doi:10.1109/TSMC.2017.2765183.

Tysse, G. and Egeland, O. Dynamic Interaction of a Heavy Crane and a Ship in Wave Motion. *Modeling, Identification and Control*, 2018. 39:45–60. doi:10.4173/mic.2018.2.1.

Tørdal, S., Olsen, J., and Hovland, G. The Norwegian Motion-Laboritory. *Modeling, Identification and Control*, 2018. 39:191–208. doi:10.4173/mic.2018.3.5.